Journal of Civil Structural Health Monitoring
https://doi.org/10.1007/s13349-024-00833-6

ORIGINAL PAPER

Predictive evaluation of dynamic responses and frequencies of bridge using optimized VMD and genetic algorithm-back propagation approach

Meng Wang[1] · Chunbao Xiong[1] · Zhi Shang[1]

Received: 21 January 2024 / Accepted: 9 July 2024

Abstract
The large amount of data collected by structural health monitoring systems deployed in the bridge contains dynamic information about the structure. To enhance the prediction accuracy of the structural dynamic responses and to evaluate the frequencies from predicted restructured responses, this paper develops an approach of optimized variational mode decomposition (OVMD) combined with a genetic algorithm-back propagation (GA-BP) neural network. The procedure is first to establish the OVMD algorithm using relative root mean square error (RRMSE) and correlation coefficient to determine reasonable decomposition and retention of the intrinsic mode function (IMF) components in the response decomposition. Then each retained IMF component is used as input to the GA-BP for prediction. Finally, the frequencies and their characteristics of the structure are estimated from the predicted restructured responses. A damaged arch bridge test shows that OVMD overcomes the shortcomings of VMD, decomposes and reconstructs the signals effectively, and outperforms the other three methods in denoising. The experimental results of the long-span cable-stayed bridge prove that OVMD combined with GA-BP has higher prediction accuracy for the dynamic responses with high sampling rates. The structural frequencies are correctly determined from predicted recombined displacement and acceleration responses. This approach provides a useful tool for bridge dynamic response decomposition, reconstruction, prediction, and structural frequency evaluation.

Keywords Long-span bridge · Dynamic response prediction · Frequency evaluation · Optimized variational mode decomposition · Genetic algorithm-back propagation neural network

1 Introduction

Bridges have become a key pivot in transportation infrastructure. Nowadays, numerous bridges are in service with the increasing sophistication of modern technology, like Hong Kong-Zhuhai-Macao Bridge, Akashi Kaikyo Bridge, and Golden Gate Bridge. However, some extreme environments may affect the safety of bridges [1, 2]. Therefore, bridge health monitoring has attracted widespread attention in recent years [3]. To ensure the proper function of bridges, it is necessary to assess the bridge structures in time.

The dynamic responses of a bridge are the results of the interaction between the external excitation and the structure, and contain various types of information about the structural state. With the development of sensor technology, a growing number of sensor monitoring systems are installed to collect structural dynamic responses. Among them, the global navigation satellite system real-time kinematic (GNSS-RTK) and accelerometers are commonly employed [4–6]. They can acquire three-dimensional displacement and acceleration of targets in real-time under almost any weather. One of the purposes of measuring response data is to identify the structural modal parameter (i.e., frequency, damping ratio, and mode shape), where the frequency is easier to obtain and is the most common modal parameter for bridge assessment. For example, Yu et al. [7] adopted a multi-positioning mode

✉ Meng Wang
engwang@tju.edu.cn

Chunbao Xiong
xcb1710737997@163.com

Zhi Shang
sz1710737997@163.com

1 School of Civil Engineering, Tianjin University, Tianjin 300350, China

Published online: 26 July 2024

GNSS system to get the displacement and frequency of a mid-span bridge. Moschas et al. [8] determined the dynamic deflections and dominant frequencies of a pedestrian bridge through multiple sensors based on GNSS and accelerometers. Xiong et al. [9] extracted the first five-order modal frequencies of a suspension bridge from the vibration monitoring data of the GNSS and accelerometer. Although GNSS and accelerometer have advantages in bridge response measurement, there are still some challenges. First, the response data (especially measured by high sampling rate sensors) is affected by noise pollution, which influences the identification of the modal parameters as well. Second, internal and external factors such as sensor failures, extreme loads, poor weather, and so on make it difficult or even impossible to collect complete response data and thus may fail to capture structural modal information.

For the first problem, nowadays the time–frequency domain analysis methods can decompose the signal responses into several discrete intrinsic mode functions (IMF) to filter the noisy components. For instance, empirical mode decomposition (EMD) [10–12], empirical wavelet transform (EWT) [13–15], empirical adaptive wavelet decomposition [16], ensemble EMD (EEMD) [17–20], complete EEMD with adaptive noise (CEEMDAN) [21–23], and variational mode decomposition (VMD) [24–27]. He et al. [28] extracted the modal frequencies of the bridge via EMD and random decrement technique. Li et al. [29] investigated the time-varying characteristics of bridge frequencies under vehicle-bridge interactions based on the improved EWT and ridge detection method. Xiao et al. [30] applied CEEMDAN to capture the bridge frequency characteristics from the acceleration response. Nevertheless, the spectral segmentation of EWT is usually susceptible to noise. One major problem with EMD is mode mixing. EEMD alleviates mode mixing but does not eliminate the added auxiliary noise, which makes it unable to reach the desired decomposition. As for CEEMDAN, although it avoids mode mixing, the emerging problem is that it decomposes redundant IMF components and leads to a lag in the information components.

Fortunately, the VMD proposed by Dragomiretskiy et al. [31] is an innovative method that decomposes the signal response into inherent IMF components. It has no mode mixing and has better robustness than EMD and other algorithms. Yang et al. [32] presented VMD with a band-pass filter to deal with the contact point response of vehicles and bridges. The study demonstrated the ability of the approach to extract structural frequencies. Mazzeo et al. [33] estimated the frequency and damping ratio of a cable-stayed bridge by VMD. The only issue with VMD is the difficulty in determining the preset number of decomposition parameter K. If a reliable and convenient criterion can be set up to decide the optimal number of K, the adaptiveness of the VMD will be enhanced. Although some studies proposed enhanced VMD algorithms, they are usually found in bearing fault diagnosis. Consequently, this study develops an improved VMD algorithm for large bridge structures.

For the second problem, machine learning algorithms are utilized for prediction to recover/increase the completeness of the response data, such as random forest [34], Bayesian [35–37], long short-term memory (LSTM) [38–41], and other neural networks [42–47], etc. Among numerous machine learning techniques [48, 49], neural networks are particularly popular in response prediction. Oh et al. [50] discussed the data recovery performance of neural networks in the numerical study and frame structure analysis. Betti et al. [51] evaluated the natural frequencies of a three-story steel frame at each damage level using artificial neural networks and genetic algorithms. However, some studies ignore whether the information that helps to assess the structural characteristics, such as modal parameters, can be extracted from the predicted response data. In other words, if the structural characteristic is not available from the predicted response data, the prediction results lose some practicality. Therefore, this paper applies the genetic algorithm-back propagation (GA-BP) neural network to the prediction of the bridge response data. Meanwhile, the predicted responses are used for modal frequency estimation to characterize the usefulness of prediction results.

Inspired by the above research, a combination approach of the optimized VMD (OVMD) and the GA-BP neural network is proposed and applied to the predictive evaluation of dynamic response and modal frequencies of a cable-stayed bridge. The OVMD algorithm aims to reduce the noise in the data and address the shortcomings of the VMD algorithm. In the GA-BP operation, to improve prediction accuracy, the selected IMF components are predicted individually to form the predicted responses. The frequency of the structure is finally estimated from the predicted restructured responses. Section 2 describes the methodology. Section 3 is a damaged arch bridge test to primarily examine the performance of OVMD. Section 4 processes the data responses of the field bridge experiment adopting the combined OVMD and GA-BP approach and performs a comparative analysis to verify the superiority of the proposed method. Section 5 summarizes the main conclusions.

2 Methodology

2.1 VMD

VMD divides the signal into a specified number of mode components, then determines the center frequency and bandwidth of different mode component signals [52].

1. The mode component signal has the following form:

$$u_k(t) = A_k(t)\cos\left[\varphi_k(t)\right] \quad (k = 1,\ 2,\ 3,\ ...,\ K) \tag{1}$$

where $u_k(t)$ is each mode component; $A_k(t)$ is the instantaneous amplitude; $\varphi_k(t)$ is the instantaneous phase.

2. The unilateral spectrum of each mode component is calculated through the Hilbert transform and is tuned to the estimated center frequency by multiplying the exponential term. The square of the signal gradient norm after frequency mixing is calculated. The bandwidth of the mode component after the frequency shift is estimated. Thus a constrained variational problem is constructed:

$$\begin{cases} \min\limits_{\{u_k\},\{\omega_k\}} \left\{ \sum\limits_{k=1}^{K} \left\| \partial_t \left[\left(\delta(t) + \frac{\mathrm{j}}{\pi t} \right) * u_k(t) \right] \mathrm{e}^{-\mathrm{j}\omega_k t} \right\|_2^2 \right\} \\ s.\ t.\ \sum\limits_{k=1}^{K} u_k(t) = f(t) \end{cases} \tag{2}$$

where $\{u_k\}$ and $\{\omega_k\}$ are the set of K mode component signals and the corresponding center frequencies; $*$ represents the convolution symbol; δ_t is the Dirac function; ∂_t denotes the partial derivative of t; $f(t)$ is the input signal response.

3. The Lagrange multiplier λ and the quadratic penalty factor α are introduced to replace the constrained variational problem with an unconstrained variational problem:

$$L(\{u_k\},\{\omega_k\},\lambda) = \alpha \sum_{k=1}^{K} \left\| \partial_t \left[\left(\delta(t) + \frac{\mathrm{j}}{\pi t} \right) * u_k(t) \right] \mathrm{e}^{-\mathrm{j}\omega_k t} \right\|_2^2 + \left\| f(t) - \sum_{k=1}^{K} u_k(t) \right\|_2^2 + \left\langle \lambda(t), f(t) - \sum_{k=1}^{K} u_k(t) \right\rangle \tag{3}$$

4. The alternating direction method of multipliers is adopted to update u_k, ω_k, and λ. Their expressions are as follows:

$$\hat{u}_k^{n+1}(\omega) = \frac{\hat{f}(\omega) - \sum_{i \neq k} \hat{u}_i(\omega) + \frac{\hat{\lambda}(\omega)}{2}}{1 + 2\alpha(\omega - \omega_k)^2} \tag{4}$$

$$\omega_k^{n+1} = \frac{\int_0^\infty \omega \left| \hat{u}_k^{n+1}(\omega) \right|^2 \mathrm{d}\omega}{\int_0^\infty \left| \hat{u}_k^{n+1}(\omega) \right|^2 \mathrm{d}\omega}, \tag{5}$$

$$\hat{\lambda}^{n+1}(\omega) = \hat{\lambda}^n(\omega) + \tau \left[\hat{f}(\omega) - \sum_{k=1}^{K} \hat{u}_k^{n+1}(\omega) \right] \tag{6}$$

where n is the number of iterations; τ is the noise tolerance; '∧' represents the Fourier transform.

5. The iteration termination condition is:

$$\sum_{k=1}^{K} \frac{\left\| \hat{u}_k^{n+1} - \hat{u}_k^n \right\|_2^2}{\left\| \hat{u}_k^n \right\|_2^2} < \varepsilon \tag{7}$$

where ε is the convergence accuracy and $\varepsilon = 10^{-7}$. Once the accuracy condition is satisfied, the K mode components, namely IMF components, are output.

2.2 OVMD

It is difficult for the VMD algorithm to set the decomposition parameter K reasonably depending on subjective experience. Improper K impacts the signal decomposition effect. In addition, the VMD only focuses on signal decomposition and does not involve signal reconstruction. Based on this, the OVMD algorithm for optimal decomposition and efficient reconstruction of signal responses is proposed. The specific steps are below:

i. Apply VMD on the input signal response and determine the IMF component with the highest correlation to the signal.

ii Compute the RRMSE to update K iteratively. When RRMSE is a local minimum value, the corresponding K is optimal. That is, the signal response is optimally decomposed into K IMF components. Otherwise, it is needed to continue updating K iteratively. The expression of RRMSE is:

$$\mathrm{RRMSE} = \sqrt{\frac{\sum_{t=1}^{N} \left[f(t) - C_{\max}\mathrm{IMF}_i(t) \right]^2}{\sum_{t=1}^{N} \left[f(t) - \bar{f} \right]^2}} \tag{8}$$

where $f(t)$ is the input signal response; $C_{\max}\mathrm{IMF}_i(t)$ denotes the IMF that has the highest correlation with $f(t)$; $\bar{f}$ is the mean value of $f(t)$.

iii As for a noisy signal, the noise is dispersed to the IMF components during the decomposition. Therefore, the correlation coefficient is presented to eliminate the noise components and choose valid IMF components to retain the signal information adequately. The correlation coefficient denotes the degree of correlation of each IMF component with the input signal response. Its expression is:

$$C = \frac{\sum_{t=1}^{N} (\mathrm{IMF}_i(t) - \overline{\mathrm{IMF}_i})(f(t) - \bar{f})}{\sqrt{\sum_{t=1}^{N} (\mathrm{IMF}_i(t) - \overline{\mathrm{IMF}_i})^2 \sum_{t=1}^{N} (f(t) - \bar{f})^2}} \tag{9}$$

where $\mathrm{IMF}_i(t)$ is each IMF component; $\overline{\mathrm{IMF}_i}$ is the average value of $\mathrm{IMF}_i(t)$.

The range of the correlation coefficient is 0 to 1. The closer the value is to 1, the stronger the correlation between the IMF and the input signal. When $0 \leq C \leq 0.3$, the IMF components are very weakly correlated with the input signal response and are considered noise-dominant components to remove. The rest of the components are retained. Figure 1 depicts the OVMD procedure.

2.3 GA-BP neural network model

BP neural network [53] is a multilayer feed-forward neural network trained by an error backpropagation algorithm. The procedure of the BP neural network is divided into two main parts, i.e., forward propagation of the sample signal and backward feedback of the error. As depicted in Fig. 2, a typical BP structure includes the input layer, the hidden layer, and the output layer. Their number of nodes is expressed as n, L, and m, respectively. The input and predicted output values are expressed as X_i ($i=1, 2, \ldots, n$) and Y_k ($k=1,2, \ldots, m$). W_{ij} and W_{jk} mean the weights.

The training procedure of the BP neural network is given below.

The BP network structure is established. The values of n, L, and m are determined; the thresholds of the hidden layer and output layer, i.e., a and b, are initialized. The learning rate and the activation function are decided. The expression of the activation function is:

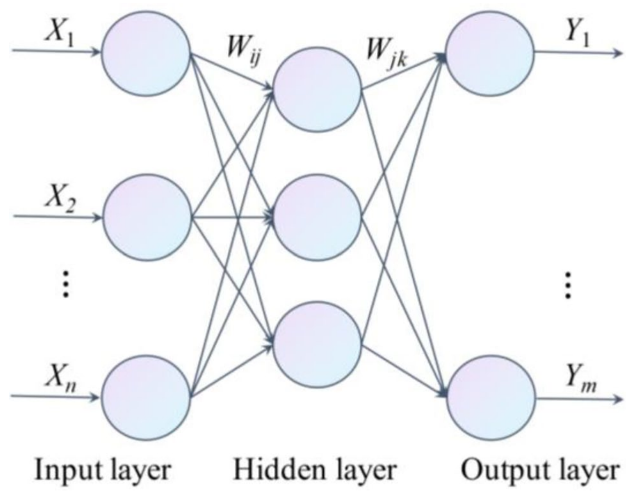

Fig. 2 BP neural network structure

$$f(x) = \frac{2}{1 + e^{-2x}} - 1 \tag{10}$$

The output H of the hidden layer is calculated:

$$H_j = f\left(\sum_{i=1}^{n} W_{ij}X_i - a_j\right) \quad (j=1,\ 2,\ \ldots,\ L) \tag{11}$$

where L is the number of hidden layer nodes.

The predicted output of the output layer Y is calculated according to H, b, and W_{jk}:

$$Y_k = \sum_{j=1}^{L} H_j W_{jk} - b_k \quad (k=1,\ 2,\ \ldots,\ m) \tag{12}$$

Fig. 1 Flowchart of the OVMD algorithm

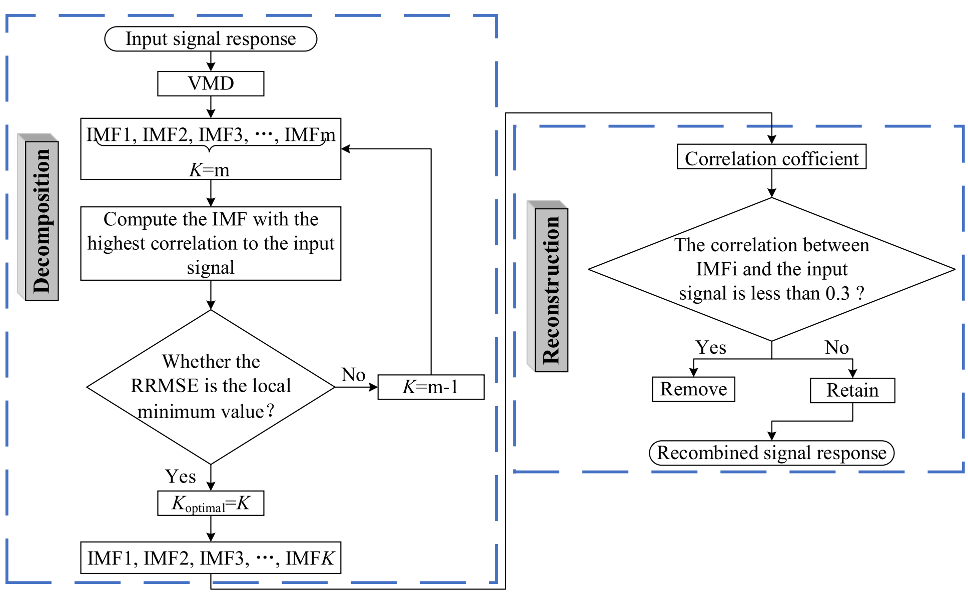

The expected output O subtracts Y to obtain the prediction error e:

$$e_k = O_k - Y_k \tag{13}$$

The weights are updated based on the prediction error:

$$W_{ij} = W_{ij} + \eta H_j(1 - H_j)X_i \sum_{k=1}^{m} W_{jk} e_k \tag{14}$$

$$W_{jk} = W_{jk} + \eta H_j e_k \tag{15}$$

where η is the learning rate.

The thresholds are updated:

$$a_j = a_j + \eta H_j(1 - H_j) \sum_{k=1}^{m} W_{jk} e_k \tag{16}$$

$$b_k = b_k + e_k \tag{17}$$

If the convergence condition is satisfied, the iteration ends. Otherwise, return to Eq. (11) and repeat the above steps.

The training process of the BP neural network is prone to trap the local optimum problem. The GA can optimize the structure of the BP model to improve its performance. In the GA-BP operation, firstly, the GA is employed to encode the initial values of weights and thresholds in the BP neural network. Subsequently, the optimal weights and thresholds are acquired by selection, crossover, and mutation. Finally, the optimal weights and thresholds from the GA are fed into the BP neural network for iterative operations to get the best prediction values. The GA-BP neural network model is shown in Fig. 3.

2.4 Framework of the proposed approach

The application of the proposed OVMD combined with the GA-BP approach in Fig. 4 includes the following steps:

(a) The measured displacement and acceleration are taken as the input signal responses.
(b) The signals are optimally decomposed based on RRMSE in the OVMD algorithm to yield a series of IMF components, and the correlation coefficient in OVMD is employed to eliminate the noisy components and retain the valid IMF components. The performance of OVMD is tested via comparative analysis.
(c) Each retained IMF component is predicted by GA-BP, and the prediction results are superimposed to form the predicted reconstructed signals.

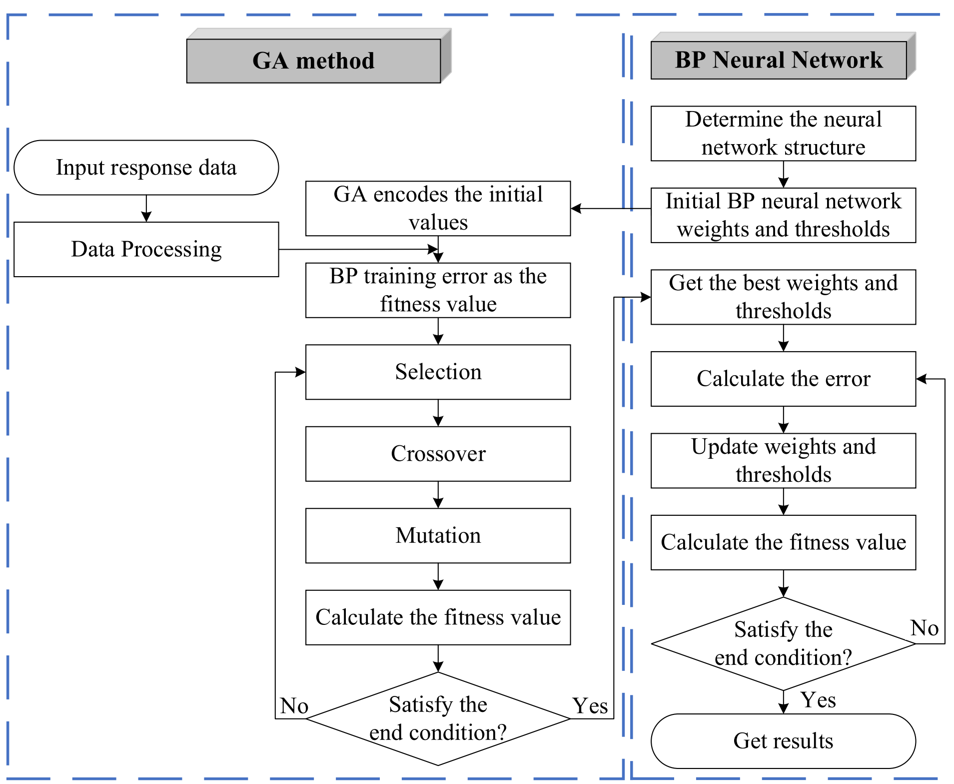

Fig. 3 GA-BP neural network model

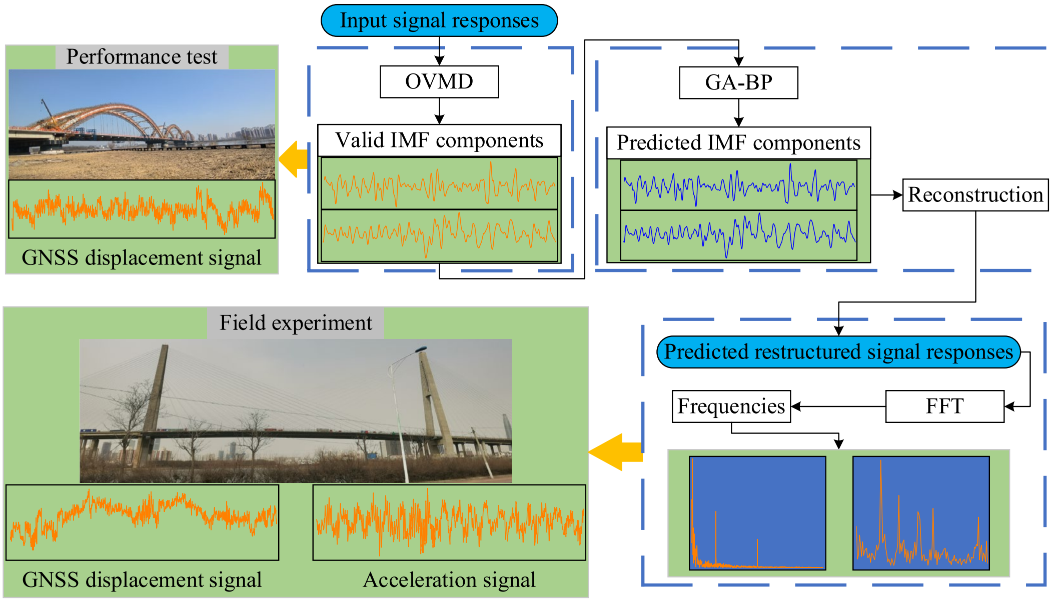

Fig. 4 Application flow of the proposed approach

Fig. 5 General view of the bridge

(d) The structural frequencies and their characteristics are evaluated from the predicted reconstructed signals by the fast Fourier transform (FFT).

3 Damaged arch bridge test

The signal's proper decomposition and reconstruction is the key to the predictive evaluation. Here, a test analysis of a damaged bridge is made before the formal experiment on the target bridge. Meanwhile, the following factors are mainly considered: (1) check the behavior of GNSS-RTK under only natural excitation (no vehicle loads) at the same sampling rate as the target bridge; (2) verify the advantages of OVMD in the decomposition and reconstruction for the actual measured signal; (3) evaluate the noise reduction effect of OVMD in strong noisy signal response.

The Rainbow Bridge, situated in Tianjin, China, was built in 1998. The overall appearance is shown in Fig. 5. The structure is a through concrete-filled steel tube arch bridge. The length of the main bridge is 504 m; the width of the longitudinal beam is 29 m, as shown in Fig. 6. On September 23, 2022, it was found that the arch foot of the structure was abnormal and part of the tie bar steel strands was broken. The bridge began repairs in September 2022 with the replacement of all load-bearing rods. The bridge reopened to traffic on June 2, 2023, after nearly 9 months of maintenance. The test was conducted on March 10, 2023, and lasted 12 h. The GNSS-RTK receiver at measuring point P in Fig. 6 as a mobile station is placed in the middle of the main span downstream of the river. The RTK sampling rate is the same as the target bridge, i.e., 50 Hz. Partial vertical displacement response is intercepted for analysis, as seen in Fig. 7.

During the test, the damaged bridge was under repair and closed to traffic. Compared with the dead weight of the structure, workers and construction vehicles on the bridge deck can be negligible. Because of the lack of vibration generated by vehicle loads, the signal in Fig. 7 is a weak dynamic displacement excited only by natural environments such as wind load and ground pulsation. Naturally, the influence of noise on the weak dynamic displacement is also more pronounced.

To attenuate the noise effect, a comparative noise reduction analysis of the displacement signal response is made employing OVMD and CEEMDAN. With the procedure of OVMD, the K is updated iteratively using RRMSE. Table 1 gives the results. When K is 7, the RRMSE shows a local minimum,

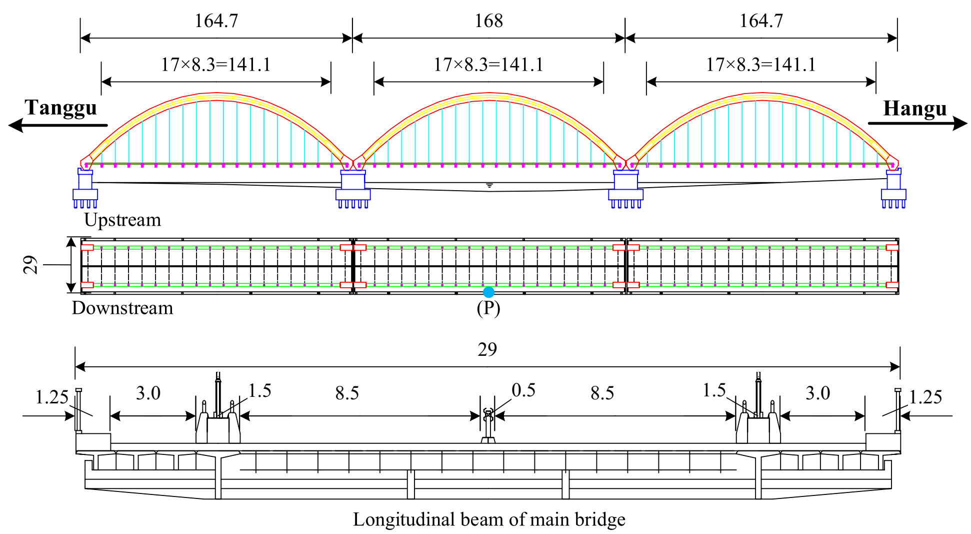

Fig. 6 Structure diagram (unit: m) and measurement point arrangement

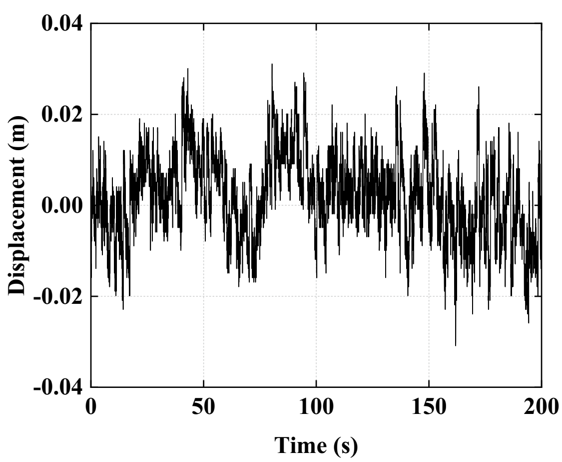

Fig. 7 Displacement signal response

which means that decomposing the signal into 7 IMF components is optimal. Simultaneously, we decompose the signal via CEEMDAN to yield 14 IMF components. The decomposition results of the two methods are depicted in Figs. 8 and 9. Obviously, CEEMDAN generates redundant IMF components; this is not conducive to the selection of valid components. In contrast, OVMD decreases the redundancy of IMF components.

Then, this paper adopts the correlation coefficient in OVMD to select the valid IMF components for reconstruction. Table 2 lists the correlation coefficients of each IMF component with the signal response in the two methods. The IMF components with correlation coefficients higher than 0.3, i.e., IMF1–IMF2 in OVMD, IMF7–IMF9 and IMF11–IMF13 in CEEMDAN, are taken as valid information and reconstructed. Furthermore, the wavelet soft threshold and EEMD-wavelet soft threshold are adopted to denoise the signal response. To estimate the performance of four methods, signal-to-noise ratio (SNR), root mean square error (RMSE), and correlation coefficient are treated as criteria. The expressions of SNR and RMSE are:

$$\mathrm{SNR} = 10\log_{10}\left\{ \frac{\sum_{t=1}^{N} x^2(t)}{\sum_{t=1}^{N} [x(t) - x'(t)]^2} \right\} \tag{18}$$

$$\mathrm{RMSE} = \sqrt{\frac{1}{N}\sum_{t=1}^{N} [x(t) - x'(t)]^2} \tag{19}$$

where $x(t)$ and $x'(t)$ denote the real signal and denoised signal. The larger the SNR, the stronger the noise reduction ability; the lower the RMSE, the smaller the signal error before and after noise reduction; the higher the correlation coefficient, the better the correlation between two sequences. As shown in Table 3, the denoised signal response after OVMD has the largest SNR (9.3209 dB), the smallest RMSE (0.0032 m), and the highest correlation (0.9374). This indicates that using the correlation coefficient presented in OVMD effectively reconstructs the signal with fewer IMF components. Also, the proposed OVMD algorithm has the best noise reduction performance.

Table 1 RRMSE values when K is iterated

K	4	5	6	7	8	9	10	11
RRMSE	0.3236	0.3231	0.4985	0.3131	0.5058	0.5045	0.5040	0.5092

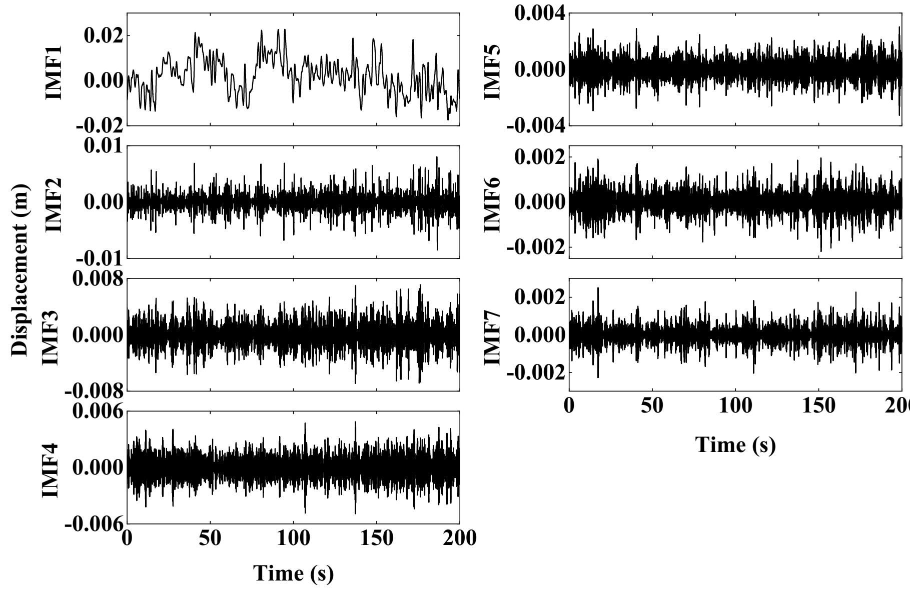

Fig. 8 OVMD decomposition

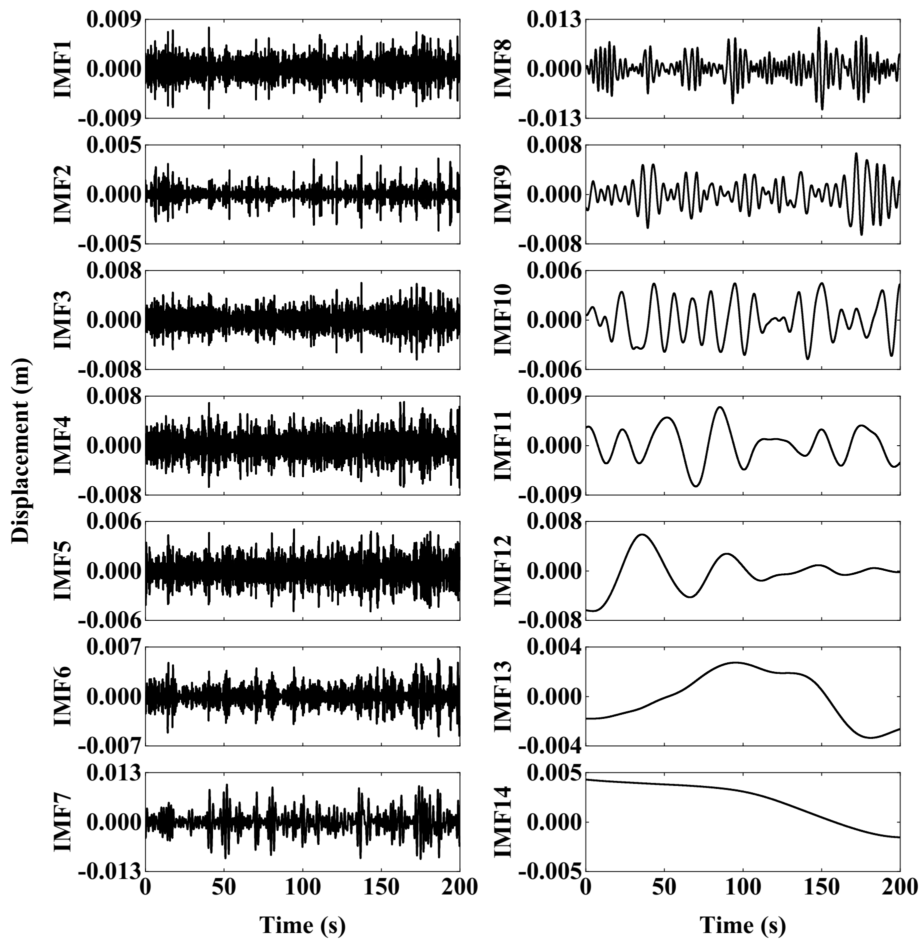

Fig. 9 CEEMDAN decomposition

The power spectral density (PSD) function of the signal reconstructed by OVMD is plotted in Fig. 10. It can be found that the first two-order frequencies (0.695 and 1 Hz) of the damaged bridge are different from those (0.6169 and 1.0960 Hz) before the damage [54]. Probably mainly structural

Table 2 Correlation coefficients of each IMF component with the displacement response

OVMD	IMF component	IMF1	IMF2	IMF3	IMF4	IMF5	IMF6	IMF7
	Correlation coefficient	0.9010	0.3587	0.2353	0.2122	0.1381	0.0935	0.0784
CEEMDAN	IMF component	IMF1	IMF2	IMF3	IMF4	IMF5	IMF6	IMF7
	Correlation coefficient	0.1506	0.1722	0.2505	0.2876	0.2443	0.2323	0.3973
	IMF component	IMF8	IMF9	IMF10	IMF11	IMF12	IMF13	IMF14
	Correlation coefficient	0.3947	0.3353	0.2728	0.4456	0.3447	0.3377	0.2920

Table 3 Performance evaluation results of different methods

Methods	SNR (dB)	RMSE (m)	Correlation coefficient
Wavelet soft threshold	5.0724	0.0052	0.8552
CEEMDAN	5.8730	0.0047	0.8879
EEMD-wavelet soft threshold	7.5923	0.0039	0.9039
OVMD	9.3209	0.0032	0.9374

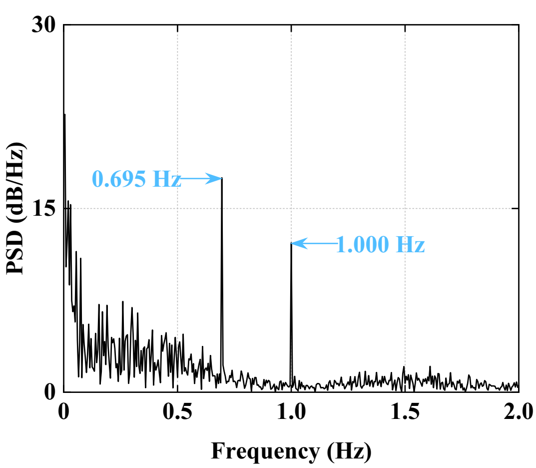

Fig. 10 PSD function detected based on OVMD

damage and lack of moving vehicles cause variations in the frequency characteristics of the bridge.

In conclusion, the damaged bridge test reveals that the GNSS-RTK with 50 Hz can obtain the structural dynamic signal response even without significant vibration excitation and extracts structural frequency based on OVMD. OVMD method facilitates the optimal decomposition and reconstruction of the signal and shows superior noise reduction capability.

4 Practical application of a long-span cable-stayed bridge

This section applied the proposed method to the predictive evaluation of the responses and frequencies of a long-span cable-stayed bridge named Haihe Bridge using GNSS-RTK and acceleration data.

4.1 Bridge overview and experimental scheme

The Haihe Bridge, located in Tianjin, China, consists of two bridges with the same structure but built in different years, as shown in Fig. 11a. The old bridge was built in 2002 and the new bridge was officially opened to traffic in 2011. Two bridges in the Haihe Bridge are single-tower double cable-stayed bridges and are reinforced concrete composite structures. Haihe Bridge has eight lanes in both directions, the main girder is 3 m high. The total lengths of the old and new bridges are 2650 and 2033 m; the spans of the two main bridges are ($310+3\times48+46$) m and ($310+2\times50+2\times40$) m; the tower heights are 167.3 and 164.8 m, respectively, as seen in Fig. 11b. Haihe Bridge has a heavy traffic flow every day. Given the old bridge was completed earlier, thus it is taken as the object of this study.

The GNSS-RTK mobile station and triaxial accelerometer with high sampling rates of 50 and 100 Hz, as displayed in Fig. 12a–b. They are positioned in the middle of the old main bridge (point M in Fig. 11b). The triaxial accelerometer is installed on the iron guardrail of the bridge sidewalk. Another GNSS receiver as a reference station (Fig. 12c) is placed on the smooth ground about 100 m away from the bridge. The erection heights of the mobile station and the reference station are 1.50 and 1.66 m, respectively. The experiment lasts from 9:00 a.m. to 6:00 p.m. on March 11, 2023, local time. In the monitoring period, the wind speed is 0.04–9.04 m/s, the temperature is 7.30–12.24 ℃, and the humidity is 25.71–43.27%RH.

4.2 OVMD processing

This study selects part of vertical GNSS displacement and acceleration dynamic signal responses for analysis. In Fig. 13, under the vehicle-dominated excitation, the

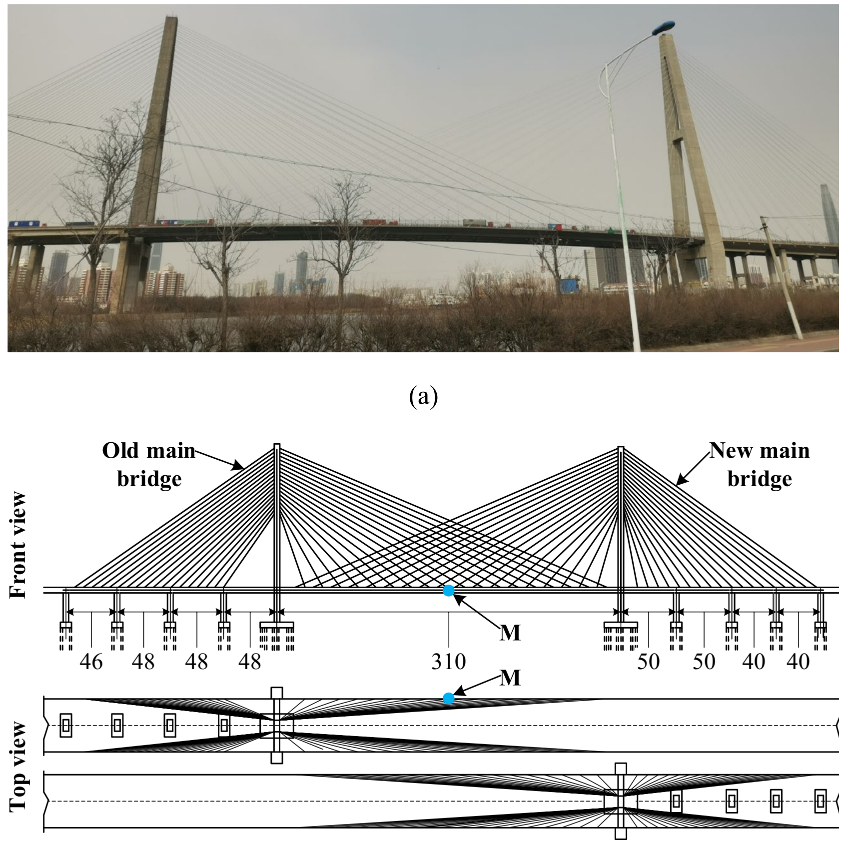

(b)

Fig. 11 Haihe Bridge: **a** panoramic view of Haihe Bridge; **b** structure schematic (unit: m) and measuring position

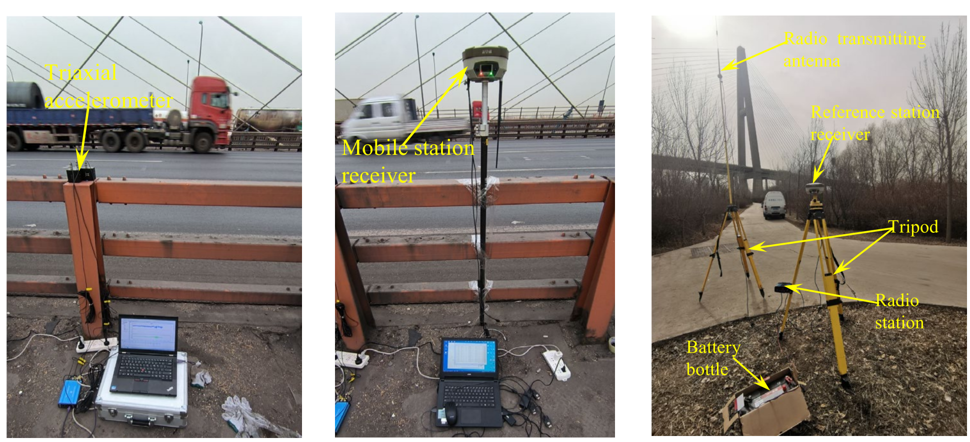

(a) (b) (c)

Fig. 12 Equipment arrangement: **a** triaxial accelerometer; **b** mobile station; and **c** reference station

displacement is – 0.0797 to 0.0563 m, and the acceleration is – 0.0334 to 0.0339 m/s^2. It is observed that two signals are subject to noise; this impacts the precision of the response prediction and frequency evaluation. The excellent performance of the OVMD is demonstrated in Sect. 3. Consequently, the OVMD algorithm is adopted to process two signal responses to determine the valid IMF components.

Following the OVMD operation rules, Table 4 illustrates the RRMSE values corresponding to different K when the two signals are decomposed. As can be seen, K is 11 and 9 are the optimal decomposition parameters because the corresponding RRMSE has local minimum values. That is, the GNSS displacement and acceleration signals are decomposed into 11 and 9 IMF components, respectively.

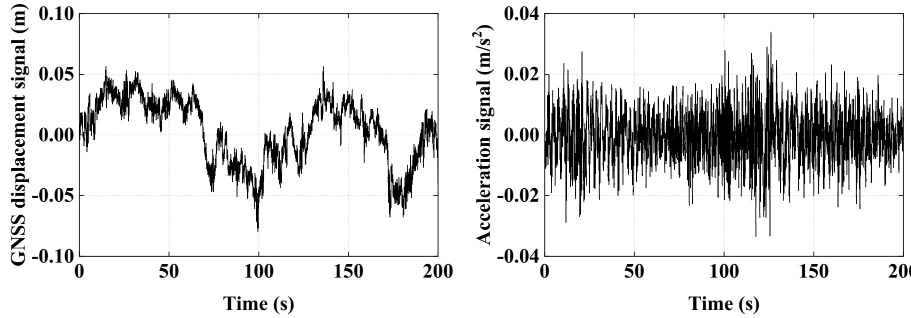

Fig. 13 Original GNSS displacement and acceleration signals

Table 4 Corresponding RRMSE values when iterating K

Displacement	K	7	8	9	10
	RRMSE	0.1712	0.1785	0.1792	0.1635
	K	11	12	13	14
	RRMSE	0.1511	0.1820	0.1522	0.1589
Acceleration	K	7	8	9	10
	RRMSE	0.6019	0.6022	0.6016	0.6341
	K	11	12	13	14
	RRMSE	0.6345	0.6344	0.6346	0.6346

The correlation coefficients between two signals and their corresponding IMF components are computed via Eq. (9), as summarized in Table 5. The IMF components with correlation coefficients greater than 0.3 are effective components, so IMF1–IMF2 decomposed from the GNSS displacement signal and IMF1–IMF3 decomposed from the acceleration signal are retained.

4.3 GA-BP prediction and analysis of dynamic signal responses

Subsequently, instead of restructuring the valid IMF components, each retained IMF component is used as the input to the GA-BP neural network. That is, the IMF components retained by OVMD are predicted using GA-BP, and then the predicted IMF components are restructured. 70% of the sample data is considered for model training, and the remaining 30% is used for test validation. The parameters in the BP neural network are set as follows: there are five hidden layers and one output layer; the number of training epochs is 2000. A learning rate of 0.001 is most appropriate. In the GA method, if the crossover probability is too large, the individuals with high fitness in the population will be destroyed due to rapid updating. But too small a value can bring the search to a standstill. Thereby, the crossover probability after attempts here is 0.7. The rest of the parameters in the GA approach are as follows: the number of evolution is 150; the population size is 60; the mutation probability is 0.05. Figures 14 and 15 display the predicted IMF components and signals reconstructed by the predicted IMF components. It can be observed that the predicted results are in good agreement with the actual ones. The noise in the predicted reconstructed signals is attenuated compared with the original signals in Fig. 13. The amplitudes of the two signals decrease, within −0.0712 to 0.0491 m and − 0.0329 to 0.0330 m/s^2, respectively.

Besides, other three methods are adopted for comparison with the proposed method. For the three cases, the signals are also first processed via OVMD. Then in method 1, the BP neural network is used to predict the retained IMF components and then reconstruct the predicted IMF components. In methods 2 and 3, BP and GA-BP neural networks are applied to predict the reconstructed signals. Namely, recombination followed by prediction. The parameters of the BP model are the same in each case. The mean error (ME), mean absolute error (MAE), mean square error (MSE), normalized root mean square error (NRMSE), and coefficient of determination (R^2) are utilized as precision indicators. Their expressions are expressed as:

Table 5 Correlation coefficients of two signals with their corresponding IMF components

Displacement	IMF component	IMF1	IMF2	IMF3	IMF4	IMF5	IMF6
	Correlation coefficient	0.9797	0.3011	0.1064	0.0871	0.0659	0.0477
	IMF component	IMF7	IMF8	IMF9	IMF10	IMF11	
	Correlation coefficient	0.0393	0.0334	0.0307	0.0291	0.0264	
Acceleration	IMF component	IMF1	IMF2	IMF3	IMF4	IMF5	IMF6
	Correlation coefficient	0.7352	0.6565	0.3710	0.1440	0.0946	0.0652
	IMF component	IMF7	IMF8	IMF9			
	Correlation coefficient	0.0375	0.0324	0.0288			

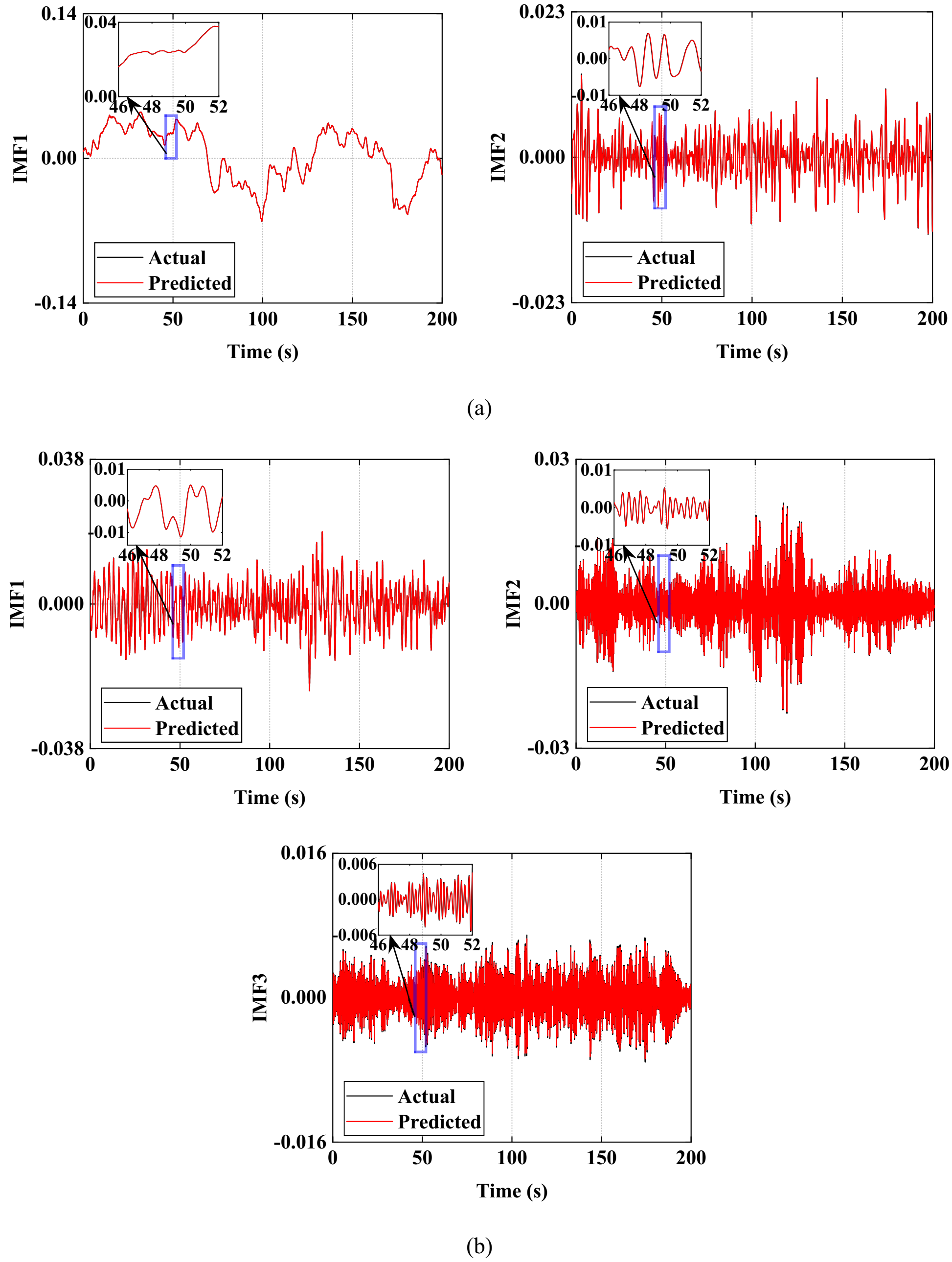

Fig. 14 Actual and predicted IMF components: **a** actual and predicted IMF components of GNSS displacement; and **b** actual and predicted IMF components of acceleration

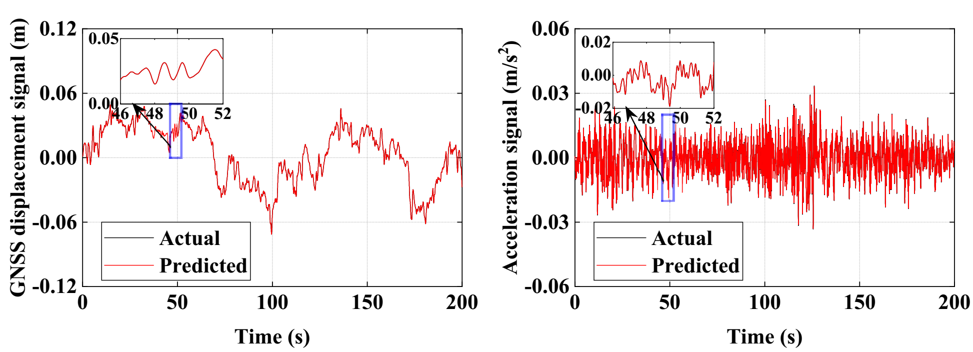

Fig. 15 Actual and predicted restructured signals

$$\mathrm{ME} = \left| \frac{1}{N} \sum_{t=1}^{N} \left[y(t) - \hat{y}(t) \right] \right|, \tag{20}$$

$$\mathrm{MAE} = \frac{1}{N} \sum_{t=1}^{N} \left| y(t) - \hat{y}(t) \right|, \tag{21}$$

$$\mathrm{MSE} = \frac{1}{N} \sum_{t=1}^{N} \left[y(t) - \hat{y}(t) \right]^2 \tag{22}$$

$$\mathrm{NRMSE} = \frac{\sqrt{\frac{1}{N} \sum_{t=1}^{N} \left[y(t) - \hat{y}(t) \right]^2}}{\max(y(t)) - \min(y(t))} \tag{23}$$

$$R^2 = 1 - \frac{\sum_{t=1}^{N} \left[y(t) - \hat{y}(t) \right]^2}{\sum_{t=1}^{N} \left[y(t) - \bar{y} \right]^2} \tag{24}$$

where $y(t)$ is the actual signal; $\hat{y}(t)$ is the predicted signal; $\bar{y}$ is the mean value of $y(t)$. The smaller the ME, MAE, MSE

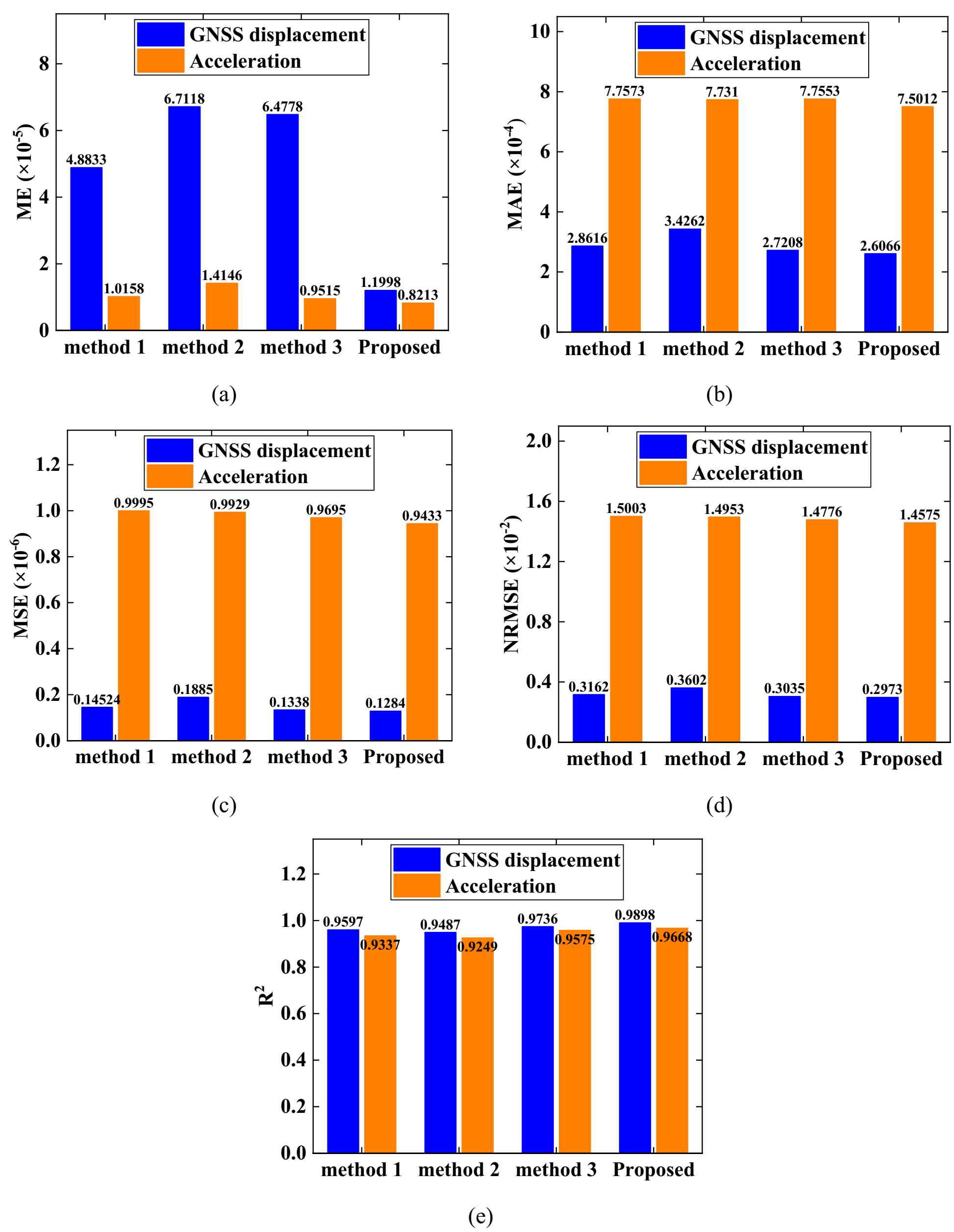

Fig. 16 Precision indicators of different methods: **a** ME; **b** MAE; **c** MSE; **d**NRMSE; and **e** R^2

and NRMSE are, and the larger the R^2 is, the better the precision is.

The prediction precision of the four methods is illustrated in Fig. 16. In general, the ME values of the predicted acceleration signal are smaller than that of the predicted GNSS displacement signal, while other indicators are the opposite. This is understandable, because the expression of ME in Eq. (20) is different from other indicators in that it is averaged before taking the absolute values. The acceleration with more sample data reduces the ME values. Notice that method 2 has the poorest indicators in the GNSS displacement prediction. In the acceleration signal prediction, method 1 appears to have the largest MAE (7.7573×10^{-4}), MSE (0.9995×10^{-6}), and NRMSE (1.5003×10^{-2}); method 2 has the largest ME (1.4146×10^{-5}) and the smallest R^2 (0.9249). In short, the prediction precision of the BP neural network (i.e., methods 1 and 2) is inferior to that of the GA-BP neural network (i.e., methods 3 and proposed). Most notably, the performance of the proposed method is the best in all indicators, especially the R^2 (0.9898) is the highest. The above indicates the proposed method has the best prediction precision.

4.4 Predictive identification and evaluation of modal frequencies

In Sect. 4.3, the signal responses (Fig. 15) reconstructed by the predicted IMF components are precisely obtained with the proposed approach. This section will detect structural modal frequencies from predicted reconstructed signal responses. The FFT is executed on the responses to get the PSD functions, as depicted in Fig. 17.

Two frequency peaks, i.e., 0.3708 and 1 Hz, are observed from the PSD function of the predicted recombined GNSS displacement signal. However, there are five frequency peaks (i.e., 0.3692, 0.6462, 0.9538, 1.1385, and 1.8308 Hz) in the PSD function of the predicted recombined acceleration signal. This implies that the predicted reconstructed GNSS displacement signal contains less structural modal information. In theory, the predicted recombined GNSS data with a sampling rate of 50 Hz has the potential to measure more modal frequencies of interest synchronously. But this may be because the vertical dynamic positioning accuracy of GNSS is not as good as that of accelerometers and makes it fail to do so in a short time. In other words, the predicted restructured acceleration contains more order modal frequencies.

In the same way, this paper summarizes the structural frequency variation characteristics identified from the predicted reconstructed signal responses, as displayed in Fig. 18. Two order frequencies statistically derived from the predicted restructured GNSS displacements vary between 0.3663–0.3758 and 0.9938–1.0038 Hz. The five order frequencies counted from the predicted restructured accelerations change between 0.3692–0.3846, 0.6462–0.6615, 0.9385–0.9692, 1.1385–1.1846, and 1.8308–1.8769 Hz. On the whole, each order frequencies vary insignificantly. In contrast to the first- and third-order frequencies in Fig. 18b, the frequencies in Fig. 18a fluctuate less, but the frequencies of the corresponding orders in the two figures have an acceptable agreement. Table 6 lists the average frequencies calculated from Fig. 18 and frequencies measured in the literature [55]. The first-order average frequency determined from the predicted restructured GNSS displacements is slightly lower than that obtained from the predicted recombined accelerations. The opposite is true for the third-order frequency. However, the difference between them is minor. The first-order average frequencies and the second-order frequency from the predicted restructured accelerations are essentially the same as the frequencies in the literature [55]. Table 6 reveals the frequencies identified from the predicted recombined signal responses have satisfactory accuracy and also reflect the usefulness of the prediction. In addition, the structural

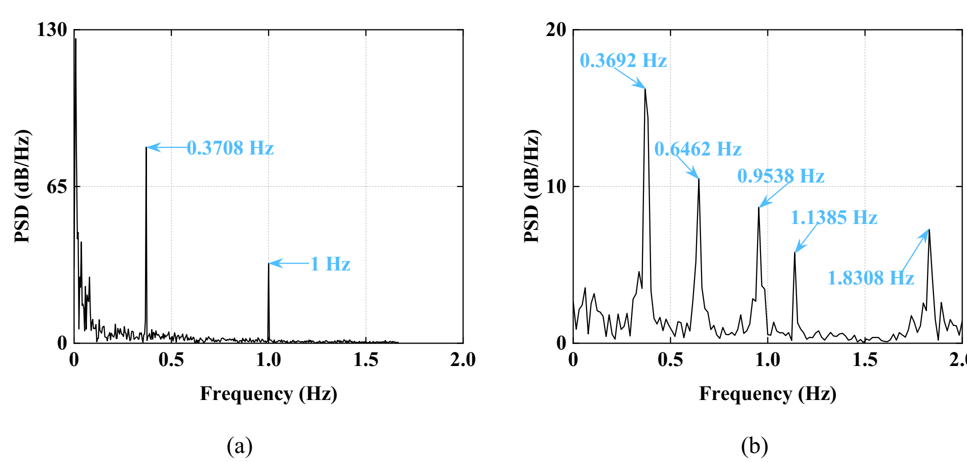

Fig. 17 PSD functions: **a** PSD function of the predicted reconstructed GNSS displacement; and **b** PSD function of the predicted reconstructed acceleration

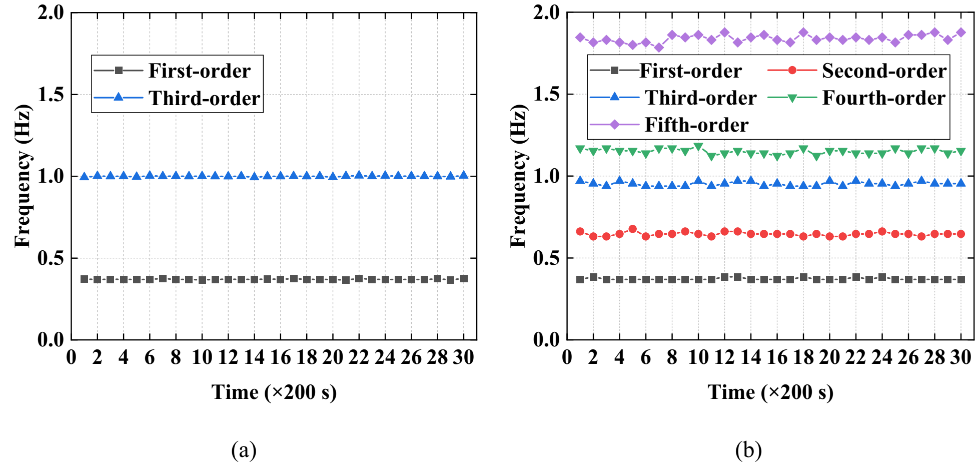

Fig. 18 Structural modal frequencies: **a** frequencies captured from the predicted reconstructed GNSS displacements; and **b** frequencies captured from the predicted reconstructed accelerations

Table 6 Statistical results of frequency evaluation

Orders	Literature [55]	This study	
		GNSS displacement response	Acceleration response
	Frequency (Hz)	Average frequency (Hz)	
First-order	0.369	0.3704	0.3723
Second-order	0.649	–	0.6457
Third-order	–	0.9996	0.9518
Fourth-order	–	–	1.1508
Fifth-order	–	–	1.8395

higher-order frequencies are captured in this study than in the literature [55].

Thus far, the precise prediction of the structural dynamic responses and the evaluation of the modal frequencies have been successfully obtained by applying the proposed approach.

5 Conclusions

In this study, an approach of OVMD combined with a GA-BP neural network is proposed for the predictive evaluation of the structural dynamic responses and frequencies based on GNSS displacement and acceleration at high sampling rates. The effectiveness of the approach was illustrated by field bridge experiments. The following conclusions are summarized:

(1) The capability of the OVMD to address the shortcomings of VMD is proven through the damaged arch bridge testing. Compared with CEEMDAN, OVMD effectively reduces the number of IMF components by optimal decomposition and realizes reasonable reconstruction of signals. Among the four methods (i.e., wavelet soft threshold, CEEMDAN, EEMD-wavelet soft threshold, and OVMD), the OVMD has the best noise reduction effect and applicability. Furthermore, the modal frequencies of the damaged bridge can be extracted from the 50 Hz GNSS-RTK displacement response handled by OVMD.

(2) The IMF components from GNSS displacements and accelerations processed by OVMD are used as inputs to GA-BP and realize the accurate prediction of dynamic responses of a long-span cable-stayed bridge. The comparative analysis indicates that the developed method enhances the prediction accuracy and its prediction indicators are better than the other three methods. This confirms the reliability and superiority of the proposed approach.

(3) The frequencies and their variation characteristics of the long-span cable-stayed bridge are determined successfully from the predicted restructured GNSS displacements and accelerations. The two-order and five-order average frequencies calculated from two predicted recombined responses are 0.3704, 0.9996 Hz and 0.3723, 0.6457, 0.9518, 1.1508, 1.8395 Hz, respectively. The frequency results are well consistent with the measurement in the previous study. Furthermore, this study detects higher-order frequencies from the predicted restructured acceleration response. The identified results reveal that the frequency estimation adopting the proposed method has satisfactory accuracy and ensures the usefulness of the predicted information.

The results obtained in this study are beneficial in providing data support for bridge health assessment. In future work, the analysis of the approach in other data sources (such as temperature and strain) or other large structures (such as super-high-rise buildings and offshore platforms) will be explored in depth to more comprehensively assess the potential integration of the proposed method.

Acknowledgements This work was supported by the National Natural Science Foundation of China (61971037). We sincerely acknowledge Tao Liu of Tianjin Surveying and Hydrography Co., Ltd. for his assistance in the experiments.

Author contributions MW: Conceptualization, Methodology, Formal analysis and investigation, Writing—original draft preparation. CX: Funding acquisition, Resources. ZS: Writing—review and editing, Data Curation.

Declarations

Conflict of interests The authors declare that there is no conflict of competing financial interests or personal relationships that could have appeared to influence the publication of this paper.

References

1. Scattarreggia N, Galik W, Calv PM, Moratti M, Orgnoni A, Pinho R (2022) Analytical and numerical analysis of the torsional response of the multi-cell deck of a collapsed cable-stayed bridge. Eng Struct 265:114412. https://doi.org/10.1016/j.engstruct.2022.114412
2. Zhao L, Cui W, Shen X, Xu S, Ding Y, Ge Y (2022) A fast on-site measure-analyze-suppress response to control vortex-induced-vibration of a long-span bridge. Structures 35:192–201. https://doi.org/10.1016/j.istruc.2021.10.017
3. Gosliga J, Hester D, Worden K, Bunce A (2022) On Population-based structural health monitoring for bridges. Mech Syst Signal Proc 173:108919. https://doi.org/10.1016/j.ymssp.2022.108919
4. Shen N, Chen L, Chen R (2022) Displacement detection based on Bayesian inference from GNSS kinematic positioning for deformation monitoring. Mech Syst Signal Proc 167:108570. https://doi.org/10.1016/j.ymssp.2021.108570
5. Xiong C, Wang M, Chen W (2022) Data analysis and dynamic characteristic investigation of large-scale civil structures monitored by RTK-GNSS based on a hybrid filtering algorithm. J Civ Struct Health Monit 12(4):857–874. https://doi.org/10.1007/s13349-022-00580-6
6. Kim K, Choi J, Chung J, Koo G, Bae IH, Sohn H (2018) Structural displacement estimation through multi-rate fusion of accelerometer and RTK-GPS displacement and velocity measurements. Measurement 130:223–235. https://doi.org/10.1016/j.measurement.2018.07.090
7. Yu J, Meng X, Shao X, Yan B, Yang L (2014) Identification of dynamic displacements and modal frequencies of a medium-span suspension bridge using multimode GNSS processing. Eng Struct 81:432–443. https://doi.org/10.1016/j.engstruct.2014.10.010
8. Moschas F, Stiros SC (2014) Three-dimensional dynamic deflections and natural frequencies of a stiff footbridge based on measurements of collocated sensors. Struct Control Health Monit 21(1):23–42. https://doi.org/10.1002/stc.1547
9. Xiong C, Lu H, Zhu J (2017) Operational modal analysis of bridge structures with data from GNSS/accelerometer measurements. Sensors 17(3):436. https://doi.org/10.3390/s17030436
10. Zhang S, Xu F, Hu M, Zhang L, Liu H, Li M (2021) A novel denoising algorithm based on TVF-EMD and its application in fault classification of rotating machinery. Measurement 179:109337. https://doi.org/10.1016/j.measurement.2021.109337
11. Nikkhoo A, Karegar H, Mohammadi RK, Hejazi F (2020) Improving the performance of the autoregressive method in modal identification of output-only systems using the empirical mode decomposition. Structures 27:1165–1173. https://doi.org/10.1016/j.istruc.2020.07.006
12. Yumnam M, Ghosh D, Gupta H (2023) Empirical mode decomposition based techniques for imaging of shallow delamination in concrete using impact echo. Mech Syst Signal Proc 184:109668. https://doi.org/10.1016/j.ymssp.2022.109668
13. Xin Y, Hao H, Li J (2019) Operational modal identification of structures based on improved empirical wavelet transform. Struct Control Health Monit 26(3):e2323. https://doi.org/10.1002/stc.2323
14. Zhong J, Bi X, Shu Q, Chen M, Zhou D, Zhang D (2020) Partial discharge signal denoising based on singular value decomposition and empirical wavelet transform. IEEE Tran Instrum Meas 69(11):8866–8873. https://doi.org/10.1109/TIM.2020.2996717
15. Mousavi AA, Zhang C, Masri SF, Gholipour G (2021) Damage detection and localization of a steel truss bridge model subjected to impact and white noise excitations using empirical wavelet transform neural network approach. Measurement 185:110060. https://doi.org/10.1016/j.measurement.2021.110060
16. Delage O, Portafaix T, Bencherif H, Bourdier A, Lagracie E (2022) Empirical adaptive wavelet decomposition (EAWD): an adaptive decomposition for the variability analysis of observation time series in atmospheric science. Nonlinear Process Geophys 29(3):265–277. https://doi.org/10.5194/npg-29-265-2022
17. Dao F, Zeng Y, Qian J (2023) A novel denoising method of the hydro-turbine runner for fault signal based on WT-EEMD. Measurement 219:113306. https://doi.org/10.1016/j.measurement.2023.113306
18. Khan I, Shan D, Li Q, Jie H (2018) Continuous modal parameter identification of cable-stayed bridges based on a novel improved ensemble empirical mode decomposition. Struct Infrastruct Eng 14(2):177–191. https://doi.org/10.1080/15732479.2017.1338734
19. Zhu L, Malekjafarian A (2019) On the use of ensemble empirical mode decomposition for the identification of bridge frequency from the responses measured in a passing vehicle. Infrastructures 4(2):32. https://doi.org/10.3390/infrastructures4020032
20. Zou Y, Chen Y, Liu P (2019) Refactoring and optimization of bridge dynamic displacement based on ensemble empirical mode decomposition. Sensors 19(14):3125. https://doi.org/10.3390/s19143125
21. Fan Q, Meng X, Nguyen DT, Xie Y, Yu J (2020) Predicting displacement of bridge based on CEEMDAN-KELM model using GNSS monitoring data. J Appl Geod 14(3):253–261. https://doi.org/10.1515/jag-2019-0057
22. Hu Y, Ouyang Y, Wang Z, Yu H, Liu L (2023) Vibration signal denoising method based on CEEMDAN and its application in brake disc unbalance detection. Mech Syst Signal Proc 187:109972. https://doi.org/10.1016/j.ymssp.2022.109972
23. Mousavi AA, Zhang C, Masri SF, Gholipour G (2022) Structural damage detection method based on the complete ensemble empirical mode decomposition with adaptive noise: a model steel truss bridge case study. Struct Health Monit 21(3):887–912. https://doi.org/10.1177/14759217211013535
24. Zhang M, Xu F (2019) Variational mode decomposition based modal parameter identification in civil engineering. Front Struct Civ Eng 13:1082–1094. https://doi.org/10.1007/s11709-019-0537-3
25. Wang C, Zhang J, Zhu HP (2020) A combined method for time-varying parameter identification based on variational mode decomposition and generalized morse wavelet. Int J Struct Stab Dyn 20(7):2050077. https://doi.org/10.1142/S0219455420500777

26. Yao XJ, Yi TH, Qu CX (2022) Autoregressive spectrum-guided variational mode decomposition for time-varying modal identification under nonstationary conditions. Eng Struct 251:113543. https://doi.org/10.1016/j.engstruct.2021.113543
27. Mousavi M, Holloway D, Olivier JC, Gandomi AH (2021) Beam damage detection using synchronisation of peaks in instantaneous frequency and amplitude of vibration data. Measurement 168:108297. https://doi.org/10.1016/j.measurement.2020.108297
28. He XH, Hua XG, Chen ZQ, Huang FL (2011) EMD-based random decrement technique for modal parameter identification of an existing railway bridge. Eng Struct 33(4):1348–1356. https://doi.org/10.1016/j.engstruct.2011.01.012
29. Li J, Guo J, Zhu X (2021) Time-varying parameter identification of bridges subject to moving vehicles using ridge extraction based on empirical wavelet transform. Int J Struct Stab Dyn 21(4):2150046. https://doi.org/10.1142/S0219455421500462
30. Xiao F, Chen GS, Zatar W, Hulsey JL (2021) Signature extraction from the dynamic responses of a bridge subjected to a moving vehicle using complete ensemble empirical mode decomposition. J Low Freq Noise Vib Act Control 40(1):278–294. https://doi.org/10.1177/1461348419872878
31. Dragomiretskiy K, Zosso D (2014) Variational mode decomposition. IEEE Trans Signal Process 62(3):531–544. https://doi.org/10.1109/TSP.2013.2288675
32. Yang YB, Xu H, Mo XQ, Wang ZL, Wu YT (2021) An effective procedure for extracting the first few bridge frequencies from a test vehicle. Acta Mech 232:1227–1251. https://doi.org/10.1007/s00707-020-02870-w
33. Mazzeo M, De Domenico D, Quaranta G, Santoro R (2023) Automatic modal identification of bridges based on free vibration response and variational mode decomposition technique. Eng Struct 280:115665. https://doi.org/10.1016/j.engstruct.2023.115665
34. Ye XW, Sun Z, Lu J (2023) Prediction and early warning of wind-induced girder and tower vibration in cable-stayed bridges with machine learning-based approach. Eng Struct 275:115261. https://doi.org/10.1016/j.engstruct.2022.115261
35. Ma Z, Yun CB, Shen YB, Yu F, Wan HP, Luo YZ (2019) Bayesian forecasting approach for structure response prediction and load effect separation of a revolving auditorium. Smart Struct Syst 24(4):507–524. https://doi.org/10.12989/sss.2019.24.4.507
36. Li M, Jia G (2020) Bayesian updating of bridge condition deterioration models using complete and incomplete inspection data. J Bridge Eng 25(3):04020007. https://doi.org/10.1061/(ASCE)BE.1943-5592.0001530
37. Ren P, Chen X, Sun L, Sun H (2021) Incremental Bayesian matrix/tensor learning for structural monitoring data imputation and response forecasting. Mech Syst Signal Proc 158:107734. https://doi.org/10.1016/j.ymssp.2021.107734
38. Guo A, Jiang A, Lin J, Li X (2020) Data mining algorithms for bridge health monitoring: Kohonen clustering and LSTM prediction approaches. J Supercomput 76(2):932–947. https://doi.org/10.1007/s11227-019-03045-8
39. Wang J, Jiang W, Li Z, Lu Y (2021) A new multi-scale sliding window LSTM framework (MSSW-LSTM): a case study for GNSS time-series prediction. Remote Sens 13(16):3328. https://doi.org/10.3390/rs13163328
40. Zhang R, Meng L, Mao Z, Sun H (2021) Spatiotemporal deep learning for bridge response forecasting. J Struct Eng 147(6):04021070. https://doi.org/10.1061/(ASCE)ST.1943-541X.0003022
41. Xin J, Zhou C, Jiang Y, Tang Q, Yang X, Zhou J (2023) A signal recovery method for bridge monitoring system using TVFEMD and encoder-decoder aided LSTM. Measurement 214:112797. https://doi.org/10.1016/j.measurement.2023.112797
42. Han X, Xiang H, Li Y, Wang Y (2019) Predictions of vertical train-bridge response using artificial neural network-based surrogate model. Adv Struct Eng 22(12):2712–2723. https://doi.org/10.1177/1369433219849809
43. Fang C, Tang H, Li Y, Wang Z (2020) Effects of random winds and waves on a long-span cross-sea bridge using Bayesian regularized back propagation neural network. Adv Struct Eng 23(4):733–748. https://doi.org/10.1177/1369433219880446
44. Li H, Wang T, Wu G (2021) Dynamic response prediction of vehicle-bridge interaction system using feedforward neural network and deep long short-term memory network. Structures 34:2415–2431. https://doi.org/10.1016/j.istruc.2021.09.008
45. Pamuncak AP, Salami MR, Adha A, Budiono B, Laory I (2021) Estimation of structural response using convolutional neural network: application to the Suramadu bridge. Eng Comput 38(10):4047–4065. https://doi.org/10.1108/EC-12-2020-0695
46. Li S, Wang W, Lu B, Du X, Dong M, Zhang T, Bai Z (2023) Long-term structural health monitoring for bridge based on back propagation neural network and long and short-term memory. Struct Health Monit 22(4):2325–2345. https://doi.org/10.1177/14759217221122337
47. Beshr AA, Zarzoura FH (2021) Using artificial neural networks for GNSS observations analysis and displacement prediction of suspension highway bridge. Innov Infrastruct Solut 6(2):109. https://doi.org/10.1007/s41062-021-00458-4
48. Afsharmovahed MH, Ghodrati Amiri G, Darvishan E (2023) A novel damage detection approach based on feature extraction and selection using machine learning without signal processing: a case study on the Tianjin Yonghe bridge. Iran J Sci Technol-Trans Civ Eng 47(6):3649–3661. https://doi.org/10.1007/s40996-023-01228-1
49. Nouri Y, Shahabian F, Shariatmadar H, Entezami A (2024) Structural damage detection in the wooden bridge using the Fourier decomposition, time series modeling and machine learning methods. J Soft Comput Civ Eng 8(2): 83–101. https://doi.org/10.22115/scce.2023.401971.1669
50. Oh BK, Glisic B, Kim Y, Park HS (2020) Convolutional neural network-based data recovery method for structural health monitoring. Struct Health Monit 19(6):1821–1838. https://doi.org/10.1177/1475921719897571
51. Betti M, Facchini L, Biagini P (2015) Damage detection on a three-storey steel frame using artificial neural networks and genetic algorithms. Meccanica 50:875–886. https://doi.org/10.1007/s11012-014-0085-9
52. Das S, Saha P (2020) Performance of hybrid decomposition algorithm under heavy noise condition for health monitoring of structure. J Civ Struct Health Monit 10(4):679–692. https://doi.org/10.1007/s13349-020-00412
53. Fu Y, Liu Y, Yang Y (2022) Multi-sensor GA-BP algorithm based gearbox fault diagnosis. Appl Sci-Basel 12(6):3106. https://doi.org/10.3390/app12063106
54. Niu Y, Ye Y, Zhao W, Shu J (2021) Dynamic monitoring and data analysis of a long-span arch bridge based on high-rate GNSS-RTK measurement combining CF-CEEMD method. J Civ Struct Health Monit 11(1):35–48. https://doi.org/10.1007/s13349-020-00436-x
55. Yu L, Xiong C, Gao Y, Zhu J (2020) Combining GNSS and accelerometer measurements for evaluation of dynamic and semi-static characteristics of bridge structures. Meas Sci Technol 31(12):125102. https://doi.org/10.1088/1361-6501/aba884